Applied Numerical Mathematics 60 (2010) 513–526

Contents lists available at ScienceDirect

Applied Numerical Mathematics

www.elsevier.com/locate/apnum

A hyperplane-constrained continuation method for near singularity in coupled nonlinear Schrödinger equations

Yueh-Cheng Kuo [a], Wen-Wei Lin [b], Shih-Feng Shieh [c], Weichung Wang [d,*]

[a] Department of Applied Mathematics, National University of Kaohsiung, Kaohsiung 811, Taiwan
[b] Department of Applied Mathematics, National Chiao Tung University, Hsinchu 300, Taiwan
[c] Department of Mathematics, National Taiwan Normal University, Taipei 116, Taiwan
[d] Department of Mathematics, National Taiwan University, Taipei 106, Taiwan

ARTICLE INFO

Article history:
Received 18 December 2008
Received in revised form 4 September 2009
Accepted 15 November 2009
Available online 18 January 2010

Keywords:
Hyperplane-constrained continuation method
Coupled nonlinear Schrödinger equations
Numerical solutions
Primal stalk solutions
Bifurcation analysis

ABSTRACT

The continuation method is a useful numerical tool for solving differential equations to obtain multiform solutions and allow bifurcation analysis. However, when a standard continuation method is used to solve a type of time-independent m-coupled nonlinear Schrödinger (NLS) equations that can be used to model nonlinear optics, nearly singular systems arise in the computations of prediction and correction search directions and detections of bifurcations. To overcome the stability and efficiency problems that exist in standard continuation methods, we propose a new hyperplane-constrained continuation method by adding additional constraints to prevent the singularities while tracking the solution curves. Aimed at the 3-coupled DNLS equations, we conduct theoretical analysis to the solutions and bifurcations on the primal stalk solution curve. The proposed algorithms have been implemented successfully to demonstrate numerical solution profiles, energies, and bifurcation diagrams in various settings.

1. Introduction

We intend to study bound state solutions of the following time-independent m-coupled nonlinear Schrödinger (NLS) equations numerically,

$$\Delta\phi_j(\mathbf{z}) - \lambda_j\phi_j(\mathbf{z}) + \mu_j\left|\phi_j(\mathbf{z})\right|^2\phi_j(\mathbf{z}) + \sum_{i\neq j,\, i=1}^{m} \beta_{ij}\left|\phi_i(\mathbf{z})\right|^2\phi_j(\mathbf{z}) = 0, \tag{1a}$$

$$\phi_j(\mathbf{z}) > 0 \quad \text{in } \mathbb{R}^n,\ j = 1,\ldots,m, \tag{1b}$$

$$\phi_j(\mathbf{z}) \to 0, \quad \text{as } |\mathbf{z}| \to \infty, \tag{1c}$$

where $\lambda_j, \mu_j > 0$ are positive constants, $n \leqslant 3$, $\beta_{ij} = \beta_{ji}$ $(i \neq j)$ are coupling coefficients, and $\mathbf{z}$ is the spatial variable. The NLS equations may be used to model a physical phenomenon in nonlinear optics [1]. In such a case, the solution ϕ_j denotes the j-th component of the beam in Kerr-like photorefractive media. The positive constant μ_j is for self-focusing in the j-th component of the beam. λ_j is referred to as the chemical potential. The coupling constant β_{ij} is the interaction between the i-th and j-th component of the beam. For $\beta_{ij} > 0$, the interaction is attractive; otherwise, the interaction is repulsive.

* Corresponding author.
E-mail addresses: yckuo@nuk.edu.tw (Y.-C. Kuo), wwlin@math.nctu.edu.tw (W.-W. Lin), sfshieh@math.ntnu.edu.tw (S.-F. Shieh), wwang@math.ntu.edu.tw (W. Wang).

0168-9274/$30.00
doi:10.1016/j.apnum.2009.11.007

To solve the NLS equations (1) numerically, we consider the corresponding m-coupled discrete nonlinear Schrödinger (DNLS) equations

$$\begin{cases} \mathbf{A}\mathbf{u}_j - \lambda_j \mathbf{u}_j + \mu_j \mathbf{u}_j^{\textcircled{2}} \circ \mathbf{u}_j + \sum_{i\neq j,\, i=1}^{m} \beta_{ij} \mathbf{u}_i^{\textcircled{2}} \circ \mathbf{u}_j = \mathbf{0}, \\ \mathbf{u}_j > 0, \quad \mathbf{u}_j \in \mathbb{R}^N, \quad \text{for } j = 1, \ldots, m, \end{cases} \tag{2}$$

where $\mathbf{u}_j \in \mathbb{R}^N$ denotes the approximation of $\phi_j(\mathbf{z})$, for $j = 1, \ldots, m$. Here, $\mathbf{A} \in \mathbb{R}^{N\times N}$ is the standard central finite difference discretization matrix of the Laplace operator with homogeneous Dirichlet boundary conditions. Additionally, it can be seen that $\mathbf{A}$ is an irreducible and symmetric negative definite matrix. The size of N depends on the computational domain and grid sizes. For example, if a uniform grid size h is applied on a square finite domain $[-d, d] \times [-d, d]$ for $n = 2$, we have $N = (\frac{2d}{h} - 1)^2$. For $\mathbf{u} = (u_1, \ldots, u_N)^\top$ and $\mathbf{v} = (v_1, \ldots, v_N)^\top \in \mathbb{R}^N$, $\mathbf{u} \circ \mathbf{v} = (u_1 v_1, \ldots, u_N v_N)^\top$ denotes the Hadamard product of $\mathbf{u}$ and $\mathbf{v}$, and $\mathbf{u}^{\textcircled{r}} = \mathbf{u} \circ \cdots \circ \mathbf{u}$ denotes the r-time Hadamard product of $\mathbf{u}$.

While continuation methods may act as an effective technique for finding multiple solutions of the NLS equations, one particular characteristic of Eq. (1) prevents standard continuation methods from being practical. Since the solution domain is unbounded in (1), a shift in any solution of the system remains a solution of the system. Consequently, a small shift in a numerical solution of an m-coupled DNLS equations (on a bounded computational domain) can also be an approximate solution to another m-coupled DNLS equations with a small residual. This phenomenon prevents classical continuation methods from being applicable or efficient for solving the target problem. First, improper prediction directions may be obtained as the prediction directions cannot be uniquely determined by numerics. Second, the Jacobian matrix may be nearly singular and the corresponding Newton's correction process becomes inaccurate and inefficient. Third, the numerical singularity also makes detections of bifurcation points difficult. Finally, these improper search directions may result in undesired solution curves in continuation methods.

Aiming at the m-coupled DNLS equations, we make the following contributions to both numerical scheme development and numerical analysis.

- To circumvent the obstacles mentioned above, we propose a novel hyperplane-constrained continuation method to compute all possible positive bound states of m-coupled DNLS equations by adding additional hyperplane constraints. By doing so, the prediction directions can be uniquely determined and the correction directions can be computed efficiently.
- Aiming at the 3-coupled DNLS equations, we characterize the primal stalk solutions and show that the primal stalk solution curve has at least $N - p$ bifurcation points at finite values of coupling constants β. Here, N is the number of grid points and p is the number of nonnegative eigenvalues of a specified matrix.
- By using the proposed hyperplane-constrained continuation method, we conduct numerical experiments to explore the versatility of numerical solutions by presenting solution profiles, bifurcation diagrams, and the corresponding energies for various settings.

The target problem has been considered in several cases. For $n = 1$, i.e. the spatial dimension is one, the system (1) is integrable. Many analytical and numerical results on solitary wave solutions of m-coupled NLS equations have been well-studied [10,14–16]. For $n = 2$ and $m = 1$, physical experiments in [22] are conducted to observe 2-dimensional photorefractive screening solutions and a 2-dimensional self-trapped beam. It is natural to believe that there are 2-dimensional m-component ($m \geqslant 2$) solutions and self-trapped beams. A general theorem for the existence of higher dimensional m-component solutions was first proved in [21]. The sign of coupling constants β_{ij}'s is crucial for the existence of ground state solutions. For $m = 3$, when all β_{ij}'s are positive, there exists a ground state solution that is radially symmetric. Furthermore, a positive bound state solution that is non-radially symmetric is also found. See [21] for details.

It is worth mentioning that if the NLS equations are equipped with trap potentials, the difficulties resulting from solution shifting no longer exist and the following numerical methods can be used to solve the equations. Bao proposed a normalized gradient flow method [3,4] and a time-splitting sine-spectral method [3]. For the time-independent case, a Gauss–Seidel-type iteration has been proposed in [9]. Furthermore, a continuation BSOR–Lanczos–Galerkin method has been developed in [8,18]. More recently, the technique of Liapunov–Schmidt reduction and continuation method has been developed in [7].

This paper is organized as follows. In Section 2, we develop a hyperplane-constrained continuation method to compute positive bound state solutions of m-coupled DNLS equations. In Section 3, we prove the existence of the bifurcation of a 3-coupled DNLS equations at finite values of the coupling constant β. Numerical results of positive bound states of some 3-coupled DNLS equations are presented in Section 4. We conclude the paper in Section 5.

Throughout this paper, we use boldfaced letters or symbols to denote a matrix or a vector. For $\mathbf{u} = (u_1, \ldots, u_N)^\top$, $[\![\mathbf{u}]\!] := \operatorname{diag}(\mathbf{u})$ denotes the diagonal matrix of $\mathbf{u}$ and $\|\mathbf{u}\|_4 = (\mathbf{u}^{\textcircled{2}\top} \mathbf{u}^{\textcircled{2}})^{1/4}$. For $\mathbf{A} \in \mathbb{R}^{N\times N}$, $\mathbf{A} > 0$ ($\geqslant 0$) denotes a positive (nonnegative) matrix with positive (nonnegative) entries, $\mathbf{A} \succ 0$ (with $\mathbf{A}^\top = \mathbf{A}$) denotes a symmetric positive definite matrix, $\sigma(\mathbf{A})$ denotes the spectrum of $\mathbf{A}$, and $\mathcal{N}(\mathbf{A})$ and $\mathcal{R}(\mathbf{A})$ denote the null and range spaces of $\mathbf{A}$, respectively. Finally, we define the energy functional

$$E(\boldsymbol{\phi}) = \sum_{j=1}^{m}\left(\frac{1}{2}\int_{\mathbb{R}^n}|\nabla\phi_j|^2 + \frac{\lambda_j}{2}\int_{\mathbb{R}^n}\phi_j^2 - \frac{\mu_j}{4}\int_{\mathbb{R}^n}\phi_j^4\right) - \frac{1}{4}\sum_{\substack{i,j=1\\ i\neq j}}^{m}\beta_{ij}\int_{\mathbb{R}^n}\phi_i^2\phi_j^2,$$

where $\boldsymbol{\phi} = (\phi_1, \ldots, \phi_m) \in (H^1(\mathbb{R}^n))^m$. The corresponding energy functional for the m-coupled DNLS equations (2) is defined as

$$E(\mathbf{x}) = \sum_{j=1}^{m}\left(-\frac{1}{2}\mathbf{u}_j^\top \mathbf{A}\mathbf{u}_j + \frac{\lambda_j}{2}\mathbf{u}_j^\top\mathbf{u}_j - \frac{\mu_j}{4}\mathbf{u}_j^{②\top}\mathbf{u}_j^{②}\right) - \frac{1}{4}\sum_{\substack{i,j=1\\ i\neq j}}^{m}\beta_{ij}\mathbf{u}_i^{②\top}\mathbf{u}_j^{②}, \tag{3}$$

where the vector $\mathbf{x} = (\mathbf{u}_1^\top, \ldots, \mathbf{u}_m^\top)^\top \in \mathbb{R}^{Nm}$.

2. The hyperplane-constrained continuation method

In this section, we develop a novel hyperplane-constrained continuation method to solve the m-coupled DNLS equations (2). We assume that the variable β_{ij} is changeable and then introduce the continuation method parameter $\beta \geqslant 0$ into Eq. (2) by rewriting

$$\beta_{ij} = \zeta_{ij}\beta \tag{4}$$

for $i, j = 1, \ldots, m$ and $i \neq j$. Here ζ_{ij}'s are nonzero constants and $\zeta_{ij} = \zeta_{ji}$. If $\zeta_{ij} > 0$, the interaction between the i-th and the j-th components is attractive; if $\zeta_{ij} < 0$, the interaction is repulsive. Furthermore, to fit the framework of a continuation method better, we rewrite the m-coupled DNLS equations (2) as

$$\mathbf{G}(\mathbf{x}, \beta) = \mathbf{0}, \tag{5a}$$

where $\mathbf{x} = (\mathbf{u}_1^\top, \ldots, \mathbf{u}_m^\top)^\top \in \mathbb{R}^{Nm}$ and $\mathbf{G} = (\mathbf{G}_1, \ldots, \mathbf{G}_m) : \mathbb{R}^{Nm} \times \mathbb{R} \to \mathbb{R}^{Nm}$ is a smooth mapping with

$$\mathbf{G}_j(\mathbf{x}, \beta) = \mathbf{A}\mathbf{u}_j - \lambda_j\mathbf{u}_j + \mu_j\mathbf{u}_j^{②} \circ \mathbf{u}_j + \beta\sum_{i\neq j,\, i=1}^{m}\zeta_{ij}\mathbf{u}_i^{②} \circ \mathbf{u}_j, \quad j = 1, \ldots, m. \tag{5b}$$

We let $\mathcal{D}\mathbf{G}$ denote the Jacobian matrix of $\mathbf{G}$; in particular,

$$\mathcal{D}\mathbf{G} = [\mathbf{G}_{\mathbf{x}}, \mathbf{G}_\beta] \in \mathbb{R}^{M\times(M+1)},$$

where $M = Nm$. We define the solution curve of (2) as

$$\mathcal{C} = \left\{\mathbf{y}(s) = \left(\mathbf{x}(s)^\top, \beta(s)\right)^\top \;\middle|\; \mathbf{G}\big(\mathbf{y}(s)\big) = \mathbf{0},\ s \in \mathbb{R}\right\}. \tag{6}$$

Here we assume a parametrization via arc-length s is available on $\mathcal{C}$. By differentiating Eq. (5) with respect to s, we obtain

$$\mathcal{D}\mathbf{G}\big(\mathbf{y}(s)\big)\dot{\mathbf{y}}(s) = \mathbf{0}, \tag{7}$$

where $\dot{\mathbf{y}}(s) = (\dot{\mathbf{x}}(s)^\top, \dot{\beta}(s))^\top$ is a tangent vector to $\mathcal{C}$ at $\mathbf{y}(s)$.

Eq. (7) suggests that the tangent vector to $\mathcal{C}$ at $\mathbf{y}(s)$ is the natural nontrivial solution of the $M \times (M+1)$ homogeneous system $\mathcal{D}\mathbf{G}(\mathbf{y}(s))\mathbf{w} = \mathbf{0}$, when $\mathcal{D}\mathbf{G}(\mathbf{y}(s))$ is of full row rank. However, if $\mathcal{D}\mathbf{G}(\mathbf{y}(s))$ is not of full rank at a certain s, then the continuation algorithm is not well defined. In this case, typical continuation methods may not follow the solution curve successfully.

The motivation for our hyperplane-constrained continuation method can be illustrated in a straightforward way by observing the NLS equation for $n = 1$ as follows. Based on the observation, we then return to the DNLS equations for $n = 2$. Afterwards, we discuss how we may circumvent the obstacle for general cases in Section 2.1.

Considering the 2-coupled NLS equations (1) with $n = 1$ and a fixed β_{12}, we differentiate both sides of (1a) with respect to the spatial variable z defined in (1c) to obtain

$$\mathbf{G}_{\mathbf{x}}\big(\mathbf{y}(s)\big)\begin{bmatrix}\phi_1'\\ \phi_2'\end{bmatrix} = \begin{bmatrix}L_1 & 2\beta_{12}\phi_1\phi_2\\ 2\beta_{12}\phi_1\phi_2 & L_2\end{bmatrix}\begin{bmatrix}\phi_1'\\ \phi_2'\end{bmatrix} = \mathbf{0}, \tag{8}$$

where $L_1 = \frac{d^2}{dz^2} - \lambda_1 + 3\mu_1\phi_1^2 + \beta_{12}\phi_2^2$ and $L_2 = \frac{d^2}{dz^2} - \lambda_2 + 3\mu_2\phi_2^2 + \beta_{12}\phi_1^2$. Eq. (8) implies that the matrix $\mathbf{G}_{\mathbf{x}}(\mathbf{y}(s))$ is actually singular with the corresponding singular vector $(\phi_1', \phi_2')^\top$. Consequently, we may have a one-dimensional solution set with tangent vector $(\phi_1', \phi_2')^\top$ of (1) for a fixed β_{12}

$$\left\{\boldsymbol{\phi}^r(x) \;\middle|\; \boldsymbol{\phi}^r(x) = \big(\phi_1(x-r), \phi_2(x-r)\big),\ r \in \mathbb{R}\right\} \tag{9}$$

that contains all the translation invariant solutions.

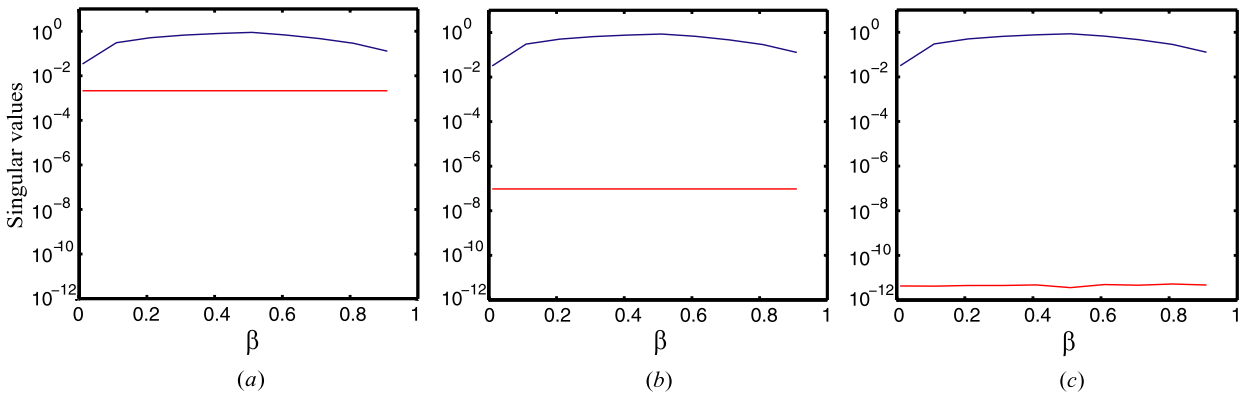

Fig. 1. Effect of "near singularity" due to computational domain size. The two smallest singular values of $\mathbf{G_x}$ of 1-dimensional 2-coupled DNLS that $\lambda_1 = \lambda_2 = 1$, $\mu_1 = \mu_2 = 1$, $\beta_{12} = \beta_{21} = \beta$ for $0 < \beta < 1$, and grid size $h = 0.2$. The computational domains are (a) $[-5, 5]$, (b) $[-10, 10]$, and (c) $[-15, 15]$.

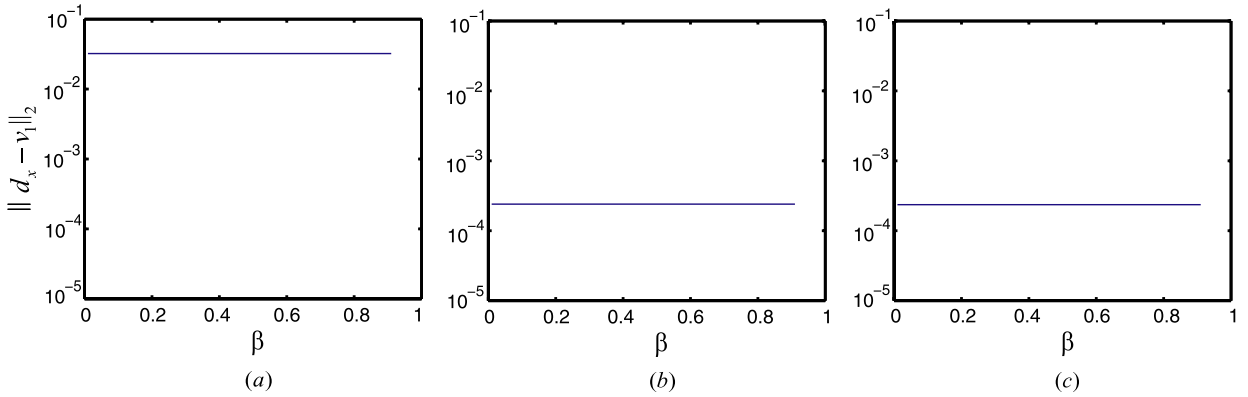

Fig. 2. The norm of difference between $\mathbf{d}_x$ and $\mathbf{v}_1$. Here $\mathbf{d}_x$ is the derivative vector and $\mathbf{v}_1$ is the singular vector of $\mathbf{G_x}$. We consider three various computational domains: (a) $[-5, 5]$; (b) $[-10, 10]$ and (c) $[-15, 15]$. Note that both $\mathbf{d}_x$ and $\mathbf{v}_1$ have been normalized before computing the differences.

To illustrate such singularity phenomena arising in the corresponding DNLS equations, we solve Eq. (2) by continuation method with $\lambda_1 = \lambda_2 = 1$, $\mu_1 = \mu_2 = 1$, $\beta_{12} = \beta_{21} = \beta$ for $0 < \beta < 1$, and grid size $h = 0.2$. The initial of the continuation method is computed by solving the decoupled DNLS using the fixed point iteration method described in [19]. Fig. 1 shows two smallest singular values of $\mathbf{G_x}$ for various β in three different computational domains. From the figure, it is clear that the second singular value is of $O(10^{-1})$ and is insignificantly dependent on domain size. In contrast, the smallest singular value decades quickly as the domain size increases. The results suggest the "near singularity" effect in numerical computations, especially in a larger computational domain. Furthermore, we verify that the singular vector $\mathbf{v}_1$ of $\mathbf{G_x}$ is close to the vector $\mathbf{d}_x$ numerically. Here $\mathbf{d}_x = [(\mathbf{D}\mathbf{u}_1)^\top, (\mathbf{D}\mathbf{u}_2)^\top]^\top$ and $\mathbf{D}$ is the discretization matrix of $\frac{d}{dx}$. Note that $\mathbf{d}_x$ is also an approximation of the vector $(\phi_1', \phi_2')^\top$ in Eq. (8) based on $\mathbf{D}$. Fig. 2 shows that $\mathbf{v}_1$ and $\mathbf{d}_x$ are getting close as the domain size increases. Note that the computed differences will decrease further in larger computational domains if we use smaller grid size h in computations. This observation will be applied while we want to rule out the singular vectors in the search directions.

Similarly, singularity can be observed in the discrete version of the m-coupled NLS equations (2) with $n = 2$. We consider a bounded domain $[-d, d] \times [-d, d]$, where the size d is sufficiently large and the uniform grid size h is sufficiently small. Let

$$\mathbf{D} = \frac{1}{2h}\begin{bmatrix} 0 & 1 & & 0 \\ -1 & \ddots & \ddots & \\ & \ddots & \ddots & 1 \\ 0 & & -1 & 0 \end{bmatrix} \in \mathbb{R}^{\sqrt{N}\times\sqrt{N}}$$

be the central difference operator. We define

$$\widehat{\mathbf{D}}_x = \mathbf{D}^\top \otimes \mathbf{I}_{\sqrt{N}}, \qquad \widehat{\mathbf{D}}_y = \mathbf{I}_{\sqrt{N}} \otimes \mathbf{D} \in \mathbb{R}^{N\times N}$$

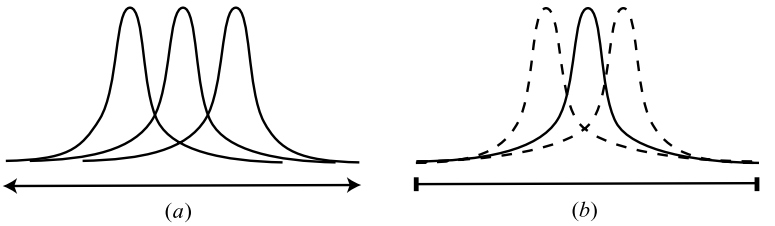

Fig. 3. Conceptual illustration of (a) translation invariant solutions and (b) ε-solutions.

as the discretization matrices of the differential operators $\frac{\partial}{\partial x}$ and $\frac{\partial}{\partial y}$, respectively. Then one can check that, similar to the operator $\frac{d}{dx}$ in (8),

$$K_s = \operatorname{span}\{\mathbf{D}_x\mathbf{x}(s), \mathbf{D}_y\mathbf{x}(s)\} \tag{10}$$

forms a numerical null space of $\mathbf{G}_{\mathbf{x}}(\mathbf{x}(s), \beta(s))$, where

$$\mathbf{D}_x = \operatorname{diag}\{\widehat{\mathbf{D}}_x, \ldots, \widehat{\mathbf{D}}_x\}, \qquad \mathbf{D}_y = \operatorname{diag}\{\widehat{\mathbf{D}}_y, \ldots, \widehat{\mathbf{D}}_y\} \in \mathbb{R}^{Nm\times Nm}.$$

In other words, $\mathbf{G}_{\mathbf{x}}(\mathbf{x}(s), \beta(s))$ is nearly singular and therefore may result in numerical difficulties in practice.

If we use $\mathbf{p} \equiv a[(\mathbf{D}_x\mathbf{x}(s))^\top, 0]^\top + b[(\mathbf{D}_y\mathbf{x}(s))^\top, 0]^\top$ $(a^2 + b^2 = 1)$ as the prediction direction, then, numerically, the "new solution" $\mathbf{x}(\tilde{s})$ $(\tilde{s} \approx s)$ computed by the continuation method is a small shift of $\mathbf{x}(s)$ in the $\mathbf{p}$-direction. These new solutions generally have very small residual $\|\mathbf{G}(\mathbf{x}(s), \beta(s))\| < \varepsilon$ and are called "ε-solutions". Note that as the domain of (2) is bounded, the residual gets larger if we keep shifting $\mathbf{x}(s)$ along the $\mathbf{p}$-direction, where $(\mathbf{x}(s), \beta(s))$ is the solution of $\mathbf{G}(\mathbf{y}(s)) = \mathbf{0}$.

The above arguments pose the following two difficulties that may be encountered by a standard continuation method. First, the near singularity may cause accuracy and efficiency problems while solving the resulting linear system. Second, a continuation method may be trapped, or become hard to keep moving ahead correctly, due to the near singularity. Fig. 3 further conceptually illustrates the effects of ε-solutions. The solid curves in part (a) of the figure represent translation invariant solutions of the NLS equations on an unbounded domain. One example is defined in (9). In contrast, no such translation invariant solution exists in exact arithmetic on a bounded computational domain. However, in a standard continuation method, any of the ε-solutions (dashed curves in part (b)) may be considered to be a reasonable approximation of the target solution (solid curve) and a particular ε-solution would be accepted as a new solution. Here, the target solution is the one that is supposed to be located on a certain solution curve being tracked. Unfortunately, the chosen solution is actually the exact solution of another solution curve. Therefore, the computed solutions may simply jump between different solution curves, rather than follow a certain solution curve.

We now summarize that such ε-solutions result in the following challenges to the prediction–correction scheme of a standard continuation method.

C1. In the prediction step, we cannot compute a unique prediction direction by solving (7).
C2. In the correction step, since the Jacobian matrix $\mathbf{G}_{\mathbf{x}}$ is nearly singular, Newton's correction will lose quadratic convergence and accuracy.
C3. The bifurcation points are difficult to detect due to the numerical singularity of the Jacobian matrix.
C4. Since the solution manifold $\mathcal{C}$ in (6) contains a 2-dimensional ε-solution set and the "good" prediction direction cannot be uniquely computed, the solutions computed by the continuation method may appear to be random or trapped in the ε-solution set. That is, we cannot follow the desired solution curve $\mathcal{C}$ in (6) efficiently by a standard continuation method.

To overcome these difficulties, we develop a hyperplane-constrained continuation method for solving (5) in the following subsections.

2.1. Prediction and correction with hyperplane constraints

Let $\mathbf{y}_i = (\mathbf{x}_i^\top, \beta_i)^\top \in \mathbb{R}^{M+1}$ be a point that has been accepted as an approximation point for the solution curve $\mathcal{C}$. A "good" prediction direction $\dot{\mathbf{y}}_i = (\dot{\mathbf{x}}_i^\top, \dot{\beta}_i)^\top$ should satisfy (7) and the vector $\dot{\mathbf{x}}_i$ at the arc-length parameter $s = s_i$ should be in $K_{s_i}^\perp$, where K_{s_i} is given in (10). It follows that the prediction direction $\dot{\mathbf{y}}_i \in \mathbb{R}^{M+1}$ should satisfy the bordered linear system

$$\begin{bmatrix} \mathbf{G}_{\mathbf{x}} & \mathbf{G}_\beta \\ \mathbf{a}_x^\top & 0 \\ \mathbf{a}_y^\top & 0 \\ \mathbf{c}_i^\top & c_i \end{bmatrix} \dot{\mathbf{y}}_i = \begin{bmatrix} \mathbf{0} \\ 0 \\ 0 \\ 1 \end{bmatrix}, \tag{11}$$

where $\mathbf{a}_x = \mathbf{D}_x\mathbf{x}_i$, $\mathbf{a}_y = \mathbf{D}_y\mathbf{x}_i$, and $(\mathbf{c}_i^\top, c_i)^\top \in \mathbb{R}^{M+1}$ is a suitable constant vector. In other words, we first use the Euler predictor

$$\mathbf{y}_{i+1,1} = \mathbf{y}_i + h_i\dot{\mathbf{y}}_i$$

to predict a new point $\mathbf{y}_{i+1,1}$, where $h_i > 0$ is the step length and $\dot{\mathbf{y}}_i$ is the unit tangent vector at $\mathbf{y}_i$ that is obtained by normalizing the solution of the bordered linear system (11). Note that Eq. (11) can be interpreted geometrically as follows. The next solution $\mathbf{y}_{i+1}$ must pass through the two hyperplanes whose normal vectors are $\mathbf{a}_x$ and $\mathbf{a}_y$. Furthermore, we accordingly coin the name "hyperplane-constrained continuation method" due to these two additional hyperplane constraints.

Now the solution curve $\mathcal{C}$ is determined by the underlying system of equations

$$\begin{cases} \mathbf{G}(\mathbf{x}, \beta) = \mathbf{0}, \\ \mathbf{a}_x^\top(\mathbf{x} - \mathbf{x}_i) = 0, \\ \mathbf{a}_y^\top(\mathbf{x} - \mathbf{x}_i) = 0, \\ \dot{\mathbf{x}}_i^\top(\mathbf{x} - \mathbf{x}_i) + \dot{\beta}_i(\beta - \beta_i) = 0. \end{cases}$$

Starting from the predictor, the accuracy of the approximation $\mathbf{y}_{i+1,1}$ to the solution curve $\mathcal{C}$ can be improved by a correction process. Typically, Newton's method is chosen as a corrector. By setting $\mathbf{y}_{i+1,l+1} = \mathbf{y}_{i+1,l} + \boldsymbol{\delta}_l$ for $l = 1, 2, \ldots$, we solve the bordered linear system

$$\begin{bmatrix} \mathbf{G}_\mathbf{x}(\mathbf{y}_{i+1,l}) & \mathbf{G}_\beta(\mathbf{y}_{i+1,l}) \\ \mathbf{a}_x^\top & 0 \\ \mathbf{a}_y^\top & 0 \\ \dot{\mathbf{x}}_i^\top & \dot{\beta}_i \end{bmatrix} \boldsymbol{\delta}_l = - \begin{bmatrix} \mathbf{G}(\mathbf{y}_{i+1,l}) \\ \rho_{x,l} \\ \rho_{y,l} \\ \rho_l \end{bmatrix}, \tag{12}$$

with $\rho_{x,l} = \mathbf{a}_x^\top(\mathbf{x}_{i+1,l} - \mathbf{x}_i)$, $\rho_{y,l} = \mathbf{a}_y^\top(\mathbf{x}_{i+1,l} - \mathbf{x}_i)$, and $\rho_l = \dot{\mathbf{y}}_i^\top(\mathbf{y}_{i+1,l} - \mathbf{y}_i)$. If $\{\mathbf{y}_{i+1,l}\}$ converges until $l = l_\infty$, then we accept $\mathbf{y}_{i+1} = \mathbf{y}_{i+1,l_\infty}$ as a new approximation to the solution curve $\mathcal{C}$.

The two linear systems (11) and (12) are overdetermined systems and can be solved by the least squares method with very small minimal residual. Another efficient way to solve (11) and (12) is to rewrite them in the form

$$\begin{cases} \begin{bmatrix} \mathbf{B} & \mathbf{f} \\ \mathbf{g}^\top & \gamma \end{bmatrix} \begin{bmatrix} \mathbf{x} \\ \sigma \end{bmatrix} = \begin{bmatrix} \mathbf{q} \\ \rho \end{bmatrix}, \\ \mathbf{x}(M+1) = \mathbf{x}(M+2) = 0, \end{cases} \tag{13}$$

where

$$\mathbf{B} = \begin{bmatrix} \mathbf{G}_\mathbf{x} & \mathbf{a}_x & \mathbf{a}_y \\ \mathbf{a}_x^\top & 0 & 0 \\ \mathbf{a}_y^\top & 0 & 0 \end{bmatrix} \in \mathbb{R}^{(M+2)\times(M+2)} \tag{14}$$

is symmetric and $\mathbf{f}, \mathbf{g}, \mathbf{q} \in \mathbb{R}^{(M+2)}$. The linear system (13) can be easily solved with the well-known block elimination (BE) algorithm (see e.g. [17]) when $\mathbf{B}$ is well-conditioned. However, near turning points or branch points, $\mathbf{B}$ in (13) becomes nearly singular, i.e., $\mathbf{B}$ is ill-conditioned. In this case, the linear system should be solved by the deflated block elimination (DBE) algorithm by Chan [6], or the more efficient and backward stable, mixed block elimination (MBE) algorithm proposed by Govaerts [13,11] as shown below.

Algorithm 1 *(Mixed block elimination).*

(i) Solve $\boldsymbol{\xi}^\top\mathbf{B} = \mathbf{g}^\top$;
(ii) Compute $\delta_1 = \gamma - \boldsymbol{\xi}^\top\mathbf{f}$, $\sigma = (\rho - \boldsymbol{\xi}^\top\mathbf{q})/\delta_1$;
(iii) Solve $\mathbf{B}\mathbf{v} = \mathbf{f}$;
(iv) Compute $\delta = \gamma - \mathbf{g}^\top\mathbf{v}$, $\mathbf{q}_1 = \mathbf{q} - \mathbf{f}\sigma$, $\rho_1 = \rho - \gamma\sigma$;
(v) Solve $\mathbf{B}\mathbf{w} = \mathbf{q}_1$;
(vi) Compute $\sigma_1 = (\rho_1 - \boldsymbol{\xi}^\top\mathbf{w})/\delta$;
(vii) Compute $\mathbf{x} = \mathbf{w} - \mathbf{v}\sigma_1$, $\sigma = \sigma + \sigma_1$.

We finally make the following remarks regarding Algorithm 1. (i) The main step in Algorithm 1 is to solve the linear system of the form $\mathbf{B}\boldsymbol{\xi} = \mathbf{g}$. (ii) Since linear systems (11) and (12) have very small minimal residuals, Eq. (13) is nearly consistent. Thus, the solution $\mathbf{x}$ solved by Algorithm 1 satisfies $\mathbf{x}(M+1) \approx \mathbf{x}(M+2) \approx 0$ automatically. In the next section, we discuss how we deal with the numerical singularity of the Jacobian matrix to find the bifurcation points.

2.2. Testing for bifurcation

Let $\mathcal{C}$ be the solution curve defined in (6), $\mathbf{y}(s) \in \mathcal{C}$ and

$$\mathbf{J}(s) = \begin{bmatrix} \mathbf{G}_{\mathbf{x}}(\mathbf{y}(s)) & \mathbf{G}_{\beta}(\mathbf{y}(s)) \\ \mathbf{a}_x^{\top} & 0 \\ \mathbf{a}_y^{\top} & 0 \end{bmatrix} \in \mathbb{R}^{(M+2)\times(M+1)}, \tag{15a}$$

$$\dot{\mathbf{J}}(s) = \begin{bmatrix} \mathbf{G}_{\mathbf{x}}(\mathbf{y}(s)) \\ \mathbf{a}_x^{\top} \\ \mathbf{a}_y^{\top} \end{bmatrix} \in \mathbb{R}^{(M+2)\times M}. \tag{15b}$$

As described in [2,12,17], a point $\mathbf{y}(s) \in \mathcal{C}$ is said to be a regular point if $\operatorname{rank}(\mathbf{J}(s)) = M$ (i.e., $\dim \mathcal{N}(\mathbf{J}(s)) = 1$) and is a singular point if $\operatorname{rank}(\mathbf{J}(s)) \leqslant M-1$ (i.e., $\dim \mathcal{N}(\mathbf{J}(s)) \geqslant 2$). For a regular point $\mathbf{y}(s)$, the tangent vector $\dot{\mathbf{y}}(s)$ is uniquely determined by the linear system (11).

Now, our task is to design an algorithm to detect singular points of the solution curve $\mathcal{C}$ and to compute tangent vectors if $\mathbf{y}(s)$ is a singular point. For simplicity, we here only consider the case that

$$\big(\mathbf{G}_{\beta}\big(\mathbf{y}(s)\big)^{\top}, 0, 0\big)^{\top} \in \mathcal{R}\big(\dot{\mathbf{J}}(s)\big) \quad \text{for each singular point } \mathbf{y}(s) \in \mathcal{C}, \tag{16}$$

i.e., $\dim \mathcal{N}(\dot{\mathbf{J}}(s)) = \dim \mathcal{N}(\mathbf{J}(s)) - 1$ and $\dim \mathcal{N}(\mathbf{J}(s)) \geqslant 2$. This case shows that the tangent vector at a singular point has a nonzero component at $\dot{\beta}(s)$ and can be expected to appear in the solution curve $\mathcal{C}$ of (5). We denote $\mathbf{B}(s)$ as the matrix $\mathbf{B}$ given by (13) at the point $\mathbf{y}(s) \in \mathcal{C}$.

Our strategy for detecting the singularity s^* of $\mathcal{C}$ is summarized in Algorithm 2. Let $s_1 < s_2$ be two consecutive continuation method parameters and $\mu(s_1)$ and $\mu(s_2)$ be the smallest eigenvalues in modulus of $\mathbf{B}(s_1)$ and $\mathbf{B}(s_2)$, respectively. It is clear that if $\mu(s_1) > 0$ and $\mu(s_2) < 0$, then there is an $s^* \in (s_1, s_2)$ such that $\mathbf{B}(s^*)$ is singular. We use the secant method to refine the interval (s_1, s_2). In the secant method loop, we use the inverse power method (in Step (ii-c)) to compute the smallest eigenvalue. After convergence, we use Algorithm 3 described in Appendix A to compute the tangent vectors at the singularity in Step (iii).

Algorithm 2 *(Detection of singularity of $\mathcal{C}$).*

(i) Given $\mu(s_i)$ the smallest eigenvalue in modulus of $\mathbf{B}(s_i)$, $i = 1, 2$, where $\mu(s_1) > 0$, $\mu(s_2) < 0$.
(ii) Perform the Secant Method until convergence:
  (a) Compute $\mathbf{y}_1(s_0) := \mathbf{y}(s_0) = \mathbf{y}(s_1) + \frac{\mathbf{t}\mu(s_1)}{\mu(s_2)-\mu(s_1)}$, where $\mathbf{t} = \mathbf{y}(s_1) - \mathbf{y}(s_2)$.
  (b) Perform the Newton Correction (12) until convergence (i.e., $\ell = \ell_\infty$), solve

$$\left[\begin{array}{cc} \mathbf{G}_{\mathbf{x}}(\mathbf{y}_\ell(s_0)) & \mathbf{G}_{\beta}(\mathbf{y}_\ell(s_0)) \\ \mathbf{a}_x^{\top} & 0 \\ \mathbf{a}_y^{\top} & 0 \\ \hline \multicolumn{2}{c}{\mathbf{t}^{\top}} \end{array}\right] \boldsymbol{\delta}_\ell = -\begin{bmatrix} \mathbf{G}(\mathbf{y}_\ell(s_0)) \\ \rho_{x,\ell} \\ \rho_{y,\ell} \\ \rho_\ell \end{bmatrix}$$

  with $\rho_{x,\ell} = [\mathbf{a}_x^{\top}, 0](\mathbf{y}_\ell(s_0) - \mathbf{y}_1(s_0))$, $\rho_{y,\ell} = [\mathbf{a}_y^{\top}, 0](\mathbf{y}_\ell(s_0) - \mathbf{y}_1(s_0))$, and $\rho_\ell = \mathbf{t}^{\top}(\mathbf{y}_\ell(s_0) - \mathbf{y}_1(s_0))$, set $\mathbf{y}_{\ell+1}(s_0) = \mathbf{y}_\ell(s_0) + \boldsymbol{\delta}_\ell$, $\ell \leftarrow \ell + 1$, go to (b).
  (c) Compute $\mu(s_0)$ of $\mathbf{B}(s_0)$ with $\mathbf{y}(s_0) = \mathbf{y}_{\ell_\infty}(s_0)$ by using the inverse power method.
  (d) If $|\mu(s_0)| < \text{Tol}$, then perform (iii), else if $\mu(s_0) > 0$, $s_1 \leftarrow s_0$, else $s_2 \leftarrow s_0$, go to (ii).
(iii) Compute the desired tangent vectors with $\mathbf{y}(s^*) = \mathbf{y}_{\ell_\infty}(s_0)$ by the methods suggested in [17, pp. 88–99].

2.3. Remarks about the method

It is worth noting that detecting the singular point of the solution curve $\mathcal{C}$ is equivalent to detecting the singularity of symmetric matrix $\mathbf{B}$ in (14). It can be shown that, provided the condition (16) holds, then the following statements are equivalent: (i) $\operatorname{rank}(\mathbf{J}(s)) \leqslant M-1$, (ii) $\mathcal{N}(\dot{\mathbf{J}}(s)) \neq \{\mathbf{0}\}$, (iii) $\mathbf{B}(s)$ is singular and there is a nonzero vector $\boldsymbol{\chi} \in \mathbb{R}^M$ such that $(\boldsymbol{\chi}^{\top}, 0, 0)^{\top} \in \mathcal{N}(\mathbf{B}(s))$. Therefore, in Step (ii-c) of Algorithm 2, instead of checking singularity of $\mathbf{J}(s)$ in (15a), we only need to check the singularity of the square symmetric matrix $\mathbf{B}(s)$ in (14).

The complexity for solving linear systems actually accounts for the main computational complexity of the proposed hyperplane-constrained continuation method. In each step of the hyperplane-constrained continuation method, it involves computations of (i) one prediction direction, (ii) several correction directions that depends on the associated convergence behavior, and (iii) test of bifurcation. Actually prediction and correction search directions can be computed by solving the linear systems in the form of (13). For the test of bifurcation, we only need to check the singularity of the matrix $\mathbf{B}(s)$ defined in (14) as mentioned above and under the assumption (16). Furthermore, as suggested in Step (ii-c) of Algorithm 2,

we can compute the smallest eigenvalue of $\mathbf{B}(s_0)$ by the inverse power method, which again requires solving the linear systems with $\mathbf{B}(s_0)$. Note that in Step (ii-b) of Algorithm 2, linear systems in the form of (12) are involved.

We have proposed a hyperplane-constrained continuation method that deals with the numerical challenges C1 to C4 listed on page 517. Specifically,

1. The prediction direction can now be computed uniquely by (11).
2. The efficiency of Newton's correction is improved, thanks to the better conditioned Jacobian matrix (12).
3. The bifurcation points can be detected accurately from (15).
4. The enhancements listed in the first two points lead to the continuation method that is capable of following the desired solution curves.

In the next section, we focus on the 3-coupled cases in both theoretical and numerical aspects. The results not only characterize the solutions of DNLS equations analytically, but demonstrate the bifurcation diagrams and visualize the theoretical predictions in Section 3.

3. Bifurcation analysis for 3-coupled discrete nonlinear Schrödinger equations

In this section, we study the 3-coupled DNLS equations theoretically by determining the corresponding primal stalk solution curve and conducting a bifurcation analysis. Note that there is no bifurcation for 1-component DNLS equations due to the uniqueness of the positive solution [20]. Furthermore, for 2-coupled DNLS equations, bifurcation analysis has been studied by Kuo, Lin, and Shieh in [18].

Lin and Wei [21] have analyzed the NLS equations (1) and the corresponding ground state solutions. Denoting $\beta_{ij} = \zeta_{ij}\beta$ (see (4)) and letting

$$\Sigma = \begin{bmatrix} 1 & |\beta_{12}| & |\beta_{13}| \\ |\beta_{12}| & 1 & |\beta_{23}| \\ |\beta_{13}| & |\beta_{23}| & 1 \end{bmatrix},$$

some of their results regarding the 3-coupled NLS equations are categorized as follows.

Case 1 *(All interactions are repulsive).* If $\zeta_{12} < 0$, $\zeta_{13} < 0$ and $\zeta_{23} < 0$, then the ground state solution does not exist.

Case 2 *(All interactions are attractive).* If $\zeta_{12} > 0$, $\zeta_{13} > 0$, $\zeta_{23} > 0$ and Σ is positive definite, then the ground state solution exists.

Case 3 *(Two repulsive and one attractive interactions).* If $\zeta_{12} < 0$, $\zeta_{13} < 0$, $\zeta_{23} > 0$ and Σ is positive definite, then the ground state solution does not exist.

Case 4 *(Two attractive and one repulsive interactions).* If $\zeta_{12} > 0$, $\zeta_{13} > 0$, $\zeta_{23} < 0$, $\beta \ll 1$ and the ground state solution exists, then it must be non-radially symmetric.

Now we use the same categories of ζ_{ij}'s and consider the solution curve $\mathcal{C}$ of (2) by letting $m = 3$ and $\lambda_1 = \lambda_2 = \lambda_3 = \mu_1 = \mu_2 = \mu_3 = 1$. As Cases 1 and 2 are straightforward, we focus on the following two particular settings of Case 3 that $\zeta_{12} = \zeta_{13} = -1$, $\zeta_{23} = 1$ and Case 4 that $\zeta_{12} = \zeta_{13} = 1$, $\zeta_{23} = -1$.

In the case that $\zeta_{12} = \zeta_{13} = -1$ and $\zeta_{23} = 1$, the 3-coupled DNLS equations of (5) become

$$\mathbf{A}\mathbf{u}_1 - \mathbf{u}_1 + \mathbf{u}_1^{③} - \beta\mathbf{u}_2^{②}\mathbf{u}_1 - \beta\mathbf{u}_3^{②}\mathbf{u}_1 = \mathbf{0}, \tag{17a}$$

$$\mathbf{A}\mathbf{u}_2 - \mathbf{u}_2 + \mathbf{u}_2^{③} - \beta\mathbf{u}_1^{②}\mathbf{u}_2 + \beta\mathbf{u}_3^{②}\mathbf{u}_2 = \mathbf{0}, \tag{17b}$$

$$\mathbf{A}\mathbf{u}_3 - \mathbf{u}_3 + \mathbf{u}_3^{③} - \beta\mathbf{u}_1^{②}\mathbf{u}_3 + \beta\mathbf{u}_2^{②}\mathbf{u}_3 = \mathbf{0}, \tag{17c}$$

where $\beta > 0$. It is clear that if we set $\beta := -\beta$, then (17) describes the 3-coupled DNLS equations for the case that $\zeta_{12} = \zeta_{13} = 1$ and $\zeta_{23} = -1$. Therefore, to investigate these two cases, we only need to consider 3-coupled DNLS equations (17) for $\beta \in \mathbb{R}$.

In the following two theorems, we first explicitly determine the solutions located on the primal stalk and then discuss how other solution curves bifurcate from the primal stalk.

Theorem 1. *The primal stalk of the solution curve*

$$\mathcal{C} = \left\{\mathbf{y}(s) = \left(\mathbf{x}^{\top}(s), \beta(s)\right)^{\top} \;\middle|\; \mathbf{G}\left(\mathbf{y}(s)\right) = \mathbf{0} \text{ is given in (17) and } s \in \mathbb{R}\right\}, \tag{18}$$

for $-\frac{1}{3} \leqslant \beta < 1$, *has the forms*

$$\mathbf{u}_1 = \left(\sqrt{\frac{1+3\beta}{1+\beta-2\beta^2}}\right)\mathbf{u}_* \quad \text{and} \quad \mathbf{u}_2 = \mathbf{u}_3 = \left(\sqrt{\frac{1+\beta}{1+\beta-2\beta^2}}\right)\mathbf{u}_*, \tag{19}$$

where $\mathbf{x}(s) = (\mathbf{u}_1^\top(s), \mathbf{u}_2^\top(s), \mathbf{u}_3^\top(s))^\top$ *and* $\mathbf{u}_*$ *is the positive solution of*

$$\mathbf{A}\mathbf{u} - \mathbf{u} + \mathbf{u}^{③} = \mathbf{0}. \tag{20}$$

Proof. By letting

$$\mathbf{u}_2 = \mathbf{u}_3 = \kappa \mathbf{u}_1 \quad \text{with } \kappa > 0, \tag{21}$$

it follows that Eqs. (17b) and (17c) are identical. Thus, equations in (17) can be reduced to

$$\begin{cases} \mathbf{A}\mathbf{u}_1 - \mathbf{u}_1 + \big(1 - 2\beta\kappa^2\big)\mathbf{u}_1^{③} = \mathbf{0}, \\ \mathbf{A}\mathbf{u}_1 - \mathbf{u}_1 + \big(\kappa^2 - \beta + \beta\kappa^2\big)\mathbf{u}_1^{③} = \mathbf{0}. \end{cases} \tag{22}$$

The system of equations in (22) has a positive solution $\mathbf{u}_1$, if $1 - 2\beta\kappa^2 = \kappa^2 - \beta + \beta\kappa^2$. This implies that

$$\kappa = \sqrt{(1+\beta)/(1+3\beta)}. \tag{23}$$

Substituting κ in (23) into the first equation of (22) we have

$$\mathbf{A}\mathbf{u}_1 - \mathbf{u}_1 + \frac{1 + \beta - 2\beta^2}{1 + 3\beta}\mathbf{u}_1^{③} = \mathbf{0}. \tag{24}$$

It can be easily verified that if $\mathbf{u}_*$ is a solution of $\mathbf{A}\mathbf{u} - \mathbf{u} + \mathbf{u}^{③} = \mathbf{0}$, then

$$\mathbf{u}_1 = \sqrt{\frac{1+3\beta}{1+\beta-2\beta^2}}\mathbf{u}_* \equiv \eta\mathbf{u}_* \tag{25}$$

solves (24).

The applicable range of β is determined by the following facts. Since $\kappa \to \sqrt{1/2}$ as $\beta \to 1^-$ (by (23)), we have

$$\mathbf{u}_2 = \mathbf{u}_3 = \kappa\mathbf{u}_1 \to \infty \tag{26}$$

by (21) and (25). On the other hand, since

$$\mathbf{u}_1 \to \mathbf{0} \quad \text{as } \beta \to -\frac{1}{3}^- \tag{27}$$

by (25), we have

$$\mathbf{u}_2 = \mathbf{u}_3 \to \sqrt{3/2}\mathbf{u}_*$$

by (17b) and (17c). □

Theorem 2. *The primal stalk described by* (19) *undergoes at least* $N - p$ *bifurcation points at finite values* $0 < \beta = \beta_q^* < 1$, $q = 1, \ldots, N - p$, *where* p *is the number of nonnegative eigenvalues of* $\mathbf{A} - \mathbf{I} + 3[\![\mathbf{u}_*^{②}]\!]$ *and* $\mathbf{u}_*$ *is the positive solution of* (20).

Proof. Since (17) has a positive solution curve $\mathbf{u}_2(\beta) = \mathbf{u}_3(\beta) = \kappa\mathbf{u}_1(\beta)$, for $0 < \beta < 1$, where κ is defined in (23), the Jacobian matrix of (17) with respect to $\mathbf{u}$ is of the form

$$\mathbf{G}_{\mathbf{u}}\big(\mathbf{y}(\beta)\big) = \begin{bmatrix} \mathbf{B}_1 & \mathbf{E}_1 & \mathbf{E}_1 \\ \mathbf{E}_1 & \mathbf{B}_2 & \mathbf{E}_2 \\ \mathbf{E}_1 & \mathbf{E}_2 & \mathbf{B}_2 \end{bmatrix},$$

where $\mathbf{B}_1 = \mathbf{A} - \mathbf{I} + [\![3\mathbf{u}_1^{②} - 2\beta\mathbf{u}_2^{②}]\!]$, $\mathbf{B}_2 = \mathbf{A} - \mathbf{I} + [\![(3+\beta)\mathbf{u}_2^{②} - \beta\mathbf{u}_1^{②}]\!]$, $\mathbf{E}_1 = -2\beta[\![\mathbf{u}_1 \circ \mathbf{u}_2]\!]$, and $\mathbf{E}_2 = 2\beta[\![\mathbf{u}_2^{②}]\!]$. From (21), (23) and (25), we have

$$\mathbf{u}_2 = \mathbf{u}_3 = \sqrt{\frac{1+\beta}{1+3\beta}}\mathbf{u}_1 = \sqrt{\frac{1+\beta}{1+\beta-2\beta^2}}\mathbf{u}_*, \tag{28}$$

where $\mathbf{u}_*$ is the positive solution of (20). Substituting (25) and (28) into $\mathbf{B}_1$, $\mathbf{B}_2$, $\mathbf{E}_1$, and $\mathbf{E}_2$, we get

$$\begin{aligned} &\mathbf{B}_1 = \mathbf{A} - \mathbf{I} + \frac{3 + 7\beta - 2\beta^2}{1 + \beta - 2\beta^2}[\![\mathbf{u}_*^{②}]\!], \qquad \mathbf{B}_2 = \mathbf{A} - \mathbf{I} + \frac{3 + 3\beta - 2\beta^2}{1 + \beta - 2\beta^2}[\![\mathbf{u}_*^{②}]\!], \\ &\mathbf{E}_1 = -2\beta\frac{\sqrt{(1+\beta)(1+3\beta)}}{1+\beta-2\beta^2}[\![\mathbf{u}_*^{②}]\!], \qquad \mathbf{E}_2 = \frac{2\beta + 2\beta^2}{1 + \beta - 2\beta^2}[\![\mathbf{u}_*^{②}]\!]. \end{aligned} \tag{29}$$

Let $\mathbf{Q}=\begin{bmatrix}\mathbf{I}&0&0\\0&\mathbf{I}&\mathbf{I}\\0&0&\mathbf{I}\end{bmatrix}$, then $\mathbf{Q}\mathbf{G}_{\mathbf{u}}(\mathbf{y}(\beta))\mathbf{Q}^{-1}=\begin{bmatrix}\mathbf{B}_1&\mathbf{E}_1&0\\2\mathbf{E}_1&\mathbf{B}_2+\mathbf{E}_2&0\\\mathbf{E}_1&\mathbf{E}_2&\mathbf{B}_2-\mathbf{E}_2\end{bmatrix}$. Hence

$$\sigma\big(\mathbf{G}_{\mathbf{u}}\big(\mathbf{y}(\beta)\big)\big)=\sigma\left(\begin{bmatrix}\mathbf{B}_1&\mathbf{E}_1\\2\mathbf{E}_1&\mathbf{B}_2+\mathbf{E}_2\end{bmatrix}\right)\cup\sigma(\mathbf{B}_2-\mathbf{E}_2). \tag{30}$$

On the other hand,

$$\begin{aligned}\begin{bmatrix}\mathbf{B}_1&\mathbf{E}_1\\2\mathbf{E}_1&\mathbf{B}_2+\mathbf{E}_2\end{bmatrix}&=\begin{bmatrix}\mathbf{B}_1&0\\0&\mathbf{B}_1\end{bmatrix}-2\beta\begin{bmatrix}0&\kappa\eta^2[\![\mathbf{u}_*^{②}]\!]\\2\kappa\eta^2[\![\mathbf{u}_*^{②}]\!]&\frac{1}{2\beta+1}[\![\mathbf{u}_*^{②}]\!]\end{bmatrix}\\&=\begin{bmatrix}1&0\\0&1\end{bmatrix}\otimes\mathbf{B}_1-\begin{bmatrix}0&1\\2&\frac{1}{(2\beta+1)\kappa\eta^2}\end{bmatrix}\otimes 2\beta\kappa\eta^2[\![\mathbf{u}_*^{②}]\!]\\&=\begin{bmatrix}1&0\\0&1\end{bmatrix}\otimes\mathbf{B}_1-\begin{bmatrix}0&1\\2&a\end{bmatrix}\otimes 2\beta\kappa\eta^2[\![\mathbf{u}_*^{②}]\!],\end{aligned} \tag{31}$$

where κ and η are given by (23) and (25), respectively, and $a=\frac{1}{(2\beta+1)\kappa\eta^2}$. Since $\frac{a+\sqrt{a^2+8}}{2}$ and $\frac{a-\sqrt{a^2+8}}{2}$ are eigenvalues of $\begin{bmatrix}0&1\\2&a\end{bmatrix}$, from (29), (30), and (31), it follows that $\sigma(\mathbf{G}_{\mathbf{u}}(\mathbf{y}(\beta)))=\Lambda_1(\beta)\cup\Lambda_2(\beta)\cup\Lambda_3(\beta)$, where

$$\begin{aligned}\Lambda_1(\beta)&=\sigma\left(\mathbf{A}-\mathbf{I}+\frac{4\beta+3}{2\beta+1}[\![\mathbf{u}_*^{②}]\!]\right),\\\Lambda_2(\beta)&=\sigma\left(\mathbf{A}-\mathbf{I}+\left[\frac{3+7\beta-2\beta^2}{1+\beta-2\beta^2}-\big(a+\sqrt{a^2+8}\big)\beta\kappa\eta^2\right][\![\mathbf{u}_*^{②}]\!]\right),\\\Lambda_3(\beta)&=\sigma\left(\mathbf{A}-\mathbf{I}+\left[\frac{3+7\beta-2\beta^2}{1+\beta-2\beta^2}-\big(a-\sqrt{a^2+8}\big)\beta\kappa\eta^2\right][\![\mathbf{u}_*^{②}]\!]\right).\end{aligned}$$

Since $(a+\sqrt{a^2+8})\beta\kappa\eta^2=-3+\frac{3+7\beta-2\beta^2}{1+\beta-2\beta^2}$, it holds that

$$\Lambda_2(\beta)=\sigma\big(\mathbf{A}-\mathbf{I}+3[\![\mathbf{u}_*^{②}]\!]\big). \tag{32}$$

Hence

$$\sigma\big(\mathbf{G}_{\mathbf{u}}\big(\mathbf{y}(\beta)\big)\big)\big|_{\beta=0}=\sigma\big(\mathbf{A}-\mathbf{I}+3[\![\mathbf{u}_*^{②}]\!]\big)\cup\sigma\big(\mathbf{A}-\mathbf{I}+3[\![\mathbf{u}_*^{②}]\!]\big)\cup\sigma\big(\mathbf{A}-\mathbf{I}+3[\![\mathbf{u}_*^{②}]\!]\big).$$

As $\beta\to 1^-$, we have that $\Lambda_1(\beta)\to\sigma(\mathbf{A}-\mathbf{I}+\frac{7}{3}[\![\mathbf{u}_*^{②}]\!])$ and $\frac{3+7\beta-2\beta^2}{1+\beta-2\beta^2}-(a-\sqrt{a^2+8})\beta\kappa\eta^2\to\infty$. So there exists a β^* with $0<\beta^*<1$ such that

$$\Lambda_3(\beta)\subset\mathbb{R}_+,\quad\text{for }\beta>\beta^*. \tag{33}$$

If the number of nonnegative eigenvalues of $\Lambda_3(0)=\sigma(\mathbf{A}-\mathbf{I}+3[\![\mathbf{u}_*^{②}]\!])$ is p, then from (32)–(33) we see that the primal stalk of the solution curve $\mathcal{C}$ of (18) undergoes at least $N-p$ bifurcation points at finite values $0<\beta_q^*<1$, $q=1,\ldots,N-p$. □

4. Numerical results

In this section, we study numerical results of positive bound state solutions for the 3-coupled DNLS equations with $\lambda_1=\lambda_2=\lambda_3=\mu_1=\mu_2=\mu_3=1$ by using the hyperplane-constrained continuation method developed in Section 2. The initial point on the primal stalk of the solution curve $\mathcal{C}$ of the 3-coupled DNLS equations is computed by the fixed point iteration method described in [19]. A squared domain $[-5,5]\times[-5,5]$ with the grid size $h=0.2$ is used in the computations. The results, including solution profiles, bifurcation diagrams, and corresponding energies, are summarized in the following two simulations.

The hyperplane-constrained continuation method program is implemented by using Fortran 95 programming language and compiled by the Intel Fortran compiler `ifort` with `O3` flag. The numerical experiments are conducted on an HP XW8000 workstation that is equipped with a 3.0 GHz CPU, 2 GB main memory, and the Red Hat Enterprise Linux 2.4.21-37.ELsmp operating system. Timing performance of the program varies with the convergence behavior of linear system solver, Newton's correction process, and detection of singularity. Roughly speaking, it usually takes around 1 or 2 minutes to move from one solution to the next one. If bifurcation test is necessary, it takes extra time, which is usually less than 10 minutes, to determine a bifurcation point.

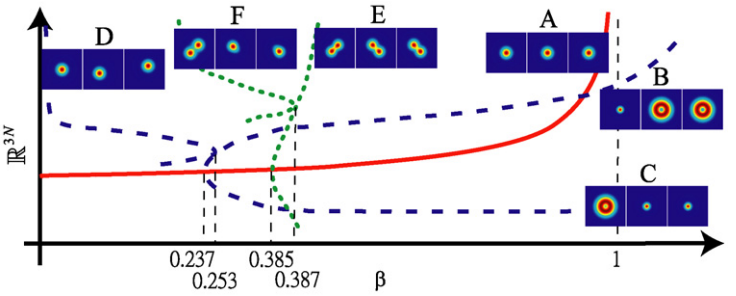

Fig. 4. Solution profiles and a bifurcation diagram of the solution curves $\mathcal{C}^+ = \{(\mathbf{x}^\top, \beta)^\top \mid \mathbf{G}(\mathbf{x}, \beta) = \mathbf{0}$ is given in (17) for $\beta \in \mathbb{R}_+\}$. (For interpretation of colors in this figure, the reader is referred to the web version of this article.)

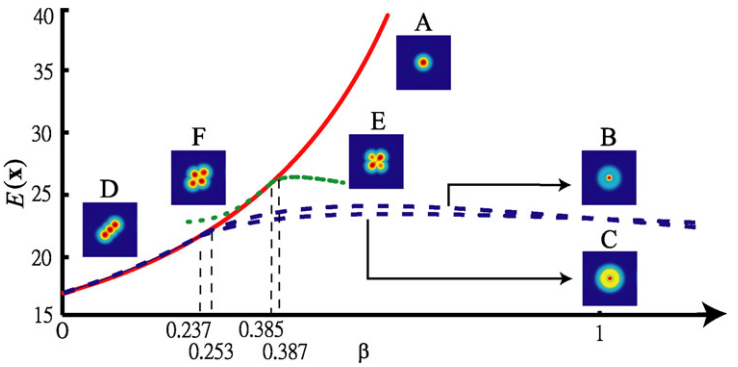

Fig. 5. Energy curves of $\mathcal{C}^+$. (For interpretation of colors in this figure, the reader is referred to the web version of this article.)

4.1. Simulation 1

We consider the case in which $\zeta_{12} = \zeta_{13} = -1$ and $\zeta_{23} = 1$. That is, we assume that one attractive and two repulsive interactions occur among the components. This setting corresponds to Case 3 in Section 3. The positive bound state solutions of the 3-coupled DNLS equations are computed and denoted by the set of solution curves

$$\mathcal{C}^+ = \left\{ \left(\mathbf{x}^\top, \beta\right)^\top \;\middle|\; \mathbf{G}(\mathbf{x}, \beta) = \mathbf{0} \text{ is given in (17) for } \beta \in \mathbb{R}_+ \right\}.$$

In Fig. 4, we plot the bifurcation diagram of the (conceptual) solution curves for $\beta \in [0, 1.2]$. The intersection points of the solution curves indicate the bifurcation points. The primal stalk solution curve, which is also described analytically in (19), is plotted by the solid red curve. The curve starts from $\beta = 0$ and bifurcates at $\beta = 0.237$ and 0.385. The solution curves bifurcated from the primal stalk while $\beta = 0.237$ are plotted as dashed blue curves. This solution curve bifurcates again at $\beta = 0.253$. On the other hand, the solution curves bifurcated from the primal stalk while $\beta = 0.385$ are plotted as dotted green curves. This solution curve bifurcates again at $\beta = 0.387$.

Furthermore, we characterize the solution curves by showing the corresponding nodal domains of three positive bound state solutions. The nodal domains are attached in triples near the solution curves. Since the forms of the solutions remain similar unless bifurcation occurs, we simply show one representative nodal domain triple for each of solution curves. Note that in each of the nodal domain triples, the left, middle and right figures are the density plots of $\mathbf{u}_1$, $\mathbf{u}_2$ and $\mathbf{u}_3$, respectively. In particular, triple A corresponds to the primal stalk (solid red curve); triples B, C, and D are associated with the dashed blue solution curves; triples E and F are associated with the dotted green solution curves.

The energy defined in (3) is computed for all solutions. In Fig. 5, we plot the energy curves corresponding to the solution curves for $\beta \in [0, 1.2]$ by using the same curve styles to indicate the corresponding solution curves. For example, the energies corresponding to the primal stalk solutions are plotted as the solid red curve. Furthermore, the nodal domains of $\mathbf{u}_1$, $\mathbf{u}_2$ and $\mathbf{u}_3$ (in the form of squared sums) are plotted in an overlapping format to show their relative positions. These overlapping nodal domains are labeled from A to F to indicate their corresponding triples presented in Fig. 4.

4.2. Simulation 2

We consider the case in which $\zeta_{12} = \zeta_{13} = 1$ and $\zeta_{23} = -1$. That is, we assume that one repulsive and two attractive interactions occur among the components (i.e. Case 4 in Section 3). The positive bound state solutions are computed and denoted by the set of solution curves

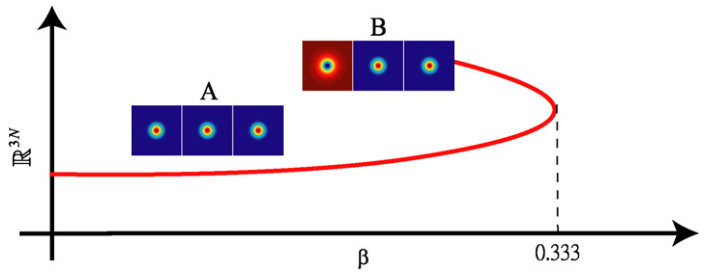

Fig. 6. Solution profiles and a bifurcation diagram of the solution curves $\mathcal{C}^- = \{(\mathbf{x}^\top, \beta)^\top \mid \mathbf{G}(\mathbf{x}, \beta) = \mathbf{0}$ is given in the 3-coupled DNLS equations with $\zeta_{12} = \zeta_{13} = 1$ and $\zeta_{23} = -1$, for $\beta \in \mathbb{R}_+\}$.

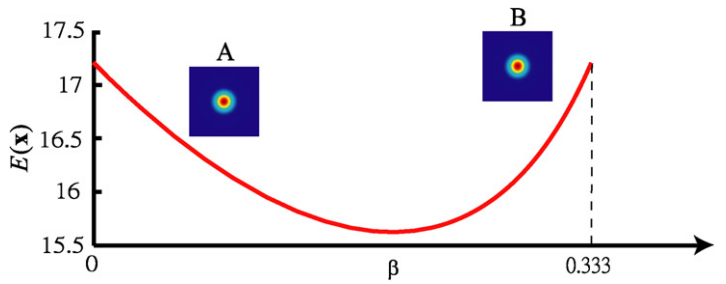

Fig. 7. Energy curve of $\mathcal{C}^-$.

$$\mathcal{C}^- = \left\{ \left(\mathbf{x}^\top, \beta\right)^\top \;\middle|\; \mathbf{G}(\mathbf{x}, \beta) = \mathbf{0} \text{ is given in the 3-coupled DNLS equations with } \zeta_{12} = \zeta_{13} = 1 \text{ and } \zeta_{23} = -1, \text{ for } \beta \in \mathbb{R}_+ \right\}.$$

We plot the bifurcation diagram and the energy curve in Figs. 6 and 7, respectively, for $\beta \in [0, 0.5]$. Similar to the results reported in Simulation 1, nodal domains of positive bound state solutions are attached near the solution curve and the energy curve. Note that there is no bifurcation in the solution curve $\mathcal{C}^-$, but a turning point is found at $\beta = 0.333$.

4.3. Remarks on the two simulations

We highlight the following observations from Simulations 1 and 2 that are consistent with the solution characters obtained from theoretical analysis.

- In Fig. 4 of Simulation 1, the β's in the primal stalk approach, but never reach, $\beta = 1$. In contrast, Fig. 6 of Simulation 2 shows that a turning point is observed on the primal stalk at $\beta = 0.333$, which corresponds to the case of $\beta = -\frac{1}{3}$ in Theorem 1.
- As shown in Fig. 5, the primal stalk energy curve (plotted as solid red) keeps rising as β increases. This phenomenon is consistent with (26).
- The computed solution profiles of $\mathcal{C}^-$ not only have the property as shown in (27), Fig. 6 further shows that the $\mathbf{u}_1$ turns to negative side after passing the turning point.
- As Theorem 2 discusses the number of bifurcation points, we note that it is proved in [21, Lemma 1] that the number of nonnegative eigenvalues of

$$\begin{cases} \Delta\phi - \phi + 3\omega_*^2\phi = \lambda\phi, \\ \phi \in H^2\left(\mathbb{R}^n\right), \end{cases}$$

is $n+1$, where ω_* is the unique solution of

$$\begin{cases} \Delta\phi - \phi + \phi^3 = 0, \\ \phi > 0 \quad \text{in } \mathbb{R}^n, \\ \omega(x) \to 0 \quad \text{as } |x| \to \infty. \end{cases}$$

In the 3-coupled DNLS equations (17) with a squared domain ($n = 2$), we can verify numerically that the number of nonnegative eigenvalues of $\Lambda_1(0) = \sigma(\mathbf{A} - \mathbf{I} + 3[\![\mathbf{u}_*^{②}]\!])$ is 3, where $\mathbf{u}_*$ is the positive solution of (20).

5. Conclusion

Aiming at the coupled DNLS equations that are discretized from the NLS equations on the whole domain, we have developed a new hyperplane-constrained continuation method. The method overcomes the numerical difficulties that prevent standard continuation methods from working or from being efficient due to the ε-solutions. We have also analyzed the primal stalk solution curve for the 3-coupled DNLS equations and we have demonstrated numerical results showing the versatility of the bound state solutions.

The proposed hyperplane-constrained continuation method can be extended to other discretization methods. For example, by using a spectral method, we may take advantage of its higher accuracy or efficiency with less grid points. However, we need to develop another suitable hyperplane for the corresponding discretization method accordingly.

Acknowledgements

We are grateful to the anonymous referee for the valuable comments and suggestions. This work is partially supported by the National Science Council, the National Center for Theoretical Sciences in Taiwan, and the Taida Institute of Mathematical Sciences.

Appendix A

Algorithm 3 *(Tangent vectors at singularity).*

(I) For $\dim\mathcal{N}(\dot{\mathbf{J}}(s^*)) = 1$:

(i) Compute the unit right null vector $\boldsymbol{\phi} = (\bar{\boldsymbol{\phi}}^\top, 0, 0)^\top$ of $\mathbf{B}(s^*)$, and solve $\dot{\mathbf{J}}(s^*)\bar{\boldsymbol{\phi}}_0 = -(\mathbf{G}_\beta(s^*)^\top, 0, 0)^\top$ with $\bar{\boldsymbol{\phi}}^\top\bar{\boldsymbol{\phi}}_0 = 0$, by using sparse SVDPACK [5] (or another suitable package);

(ii) Form $\boldsymbol{\phi}_1 = \begin{pmatrix}\bar{\boldsymbol{\phi}}\\ 0\end{pmatrix}$ and $\boldsymbol{\phi}_2 = \begin{pmatrix}\bar{\boldsymbol{\phi}}_0\\ 1\end{pmatrix}$;

(iii) Solve the real vector roots $\{(\hat{\mu}_k, \hat{\nu}_k)\}_{k=1}^2$ of $a_{11}\mu^2 + 2a_{12}\mu\nu + a_{22}\nu^2$ with

$$a_{11} = \bar{\boldsymbol{\phi}}^\top\mathbf{G}_{\mathbf{xx}}(s^*)\bar{\boldsymbol{\phi}}\bar{\boldsymbol{\phi}}, \qquad a_{12} = \bar{\boldsymbol{\phi}}^\top\big[\mathbf{G}_{\mathbf{xx}}(s^*)\bar{\boldsymbol{\phi}}_0 + \mathbf{G}_{\mathbf{x}\beta}\big]\bar{\boldsymbol{\phi}},$$
$$a_{22} = \bar{\boldsymbol{\phi}}^\top\big[\mathbf{G}_{\mathbf{xx}}(s^*)\bar{\boldsymbol{\phi}}_0\bar{\boldsymbol{\phi}}_0 + 2\mathbf{G}_{\mathbf{x}\beta}(s^*)\bar{\boldsymbol{\phi}}_0 + \mathbf{G}_{\beta\beta}(s^*)\big];$$

(iv) Form tangent vectors $\dot{\mathbf{y}}_k(s^*) = \hat{\mu}_k\boldsymbol{\phi}_1 + \hat{\nu}_k\boldsymbol{\phi}_2$, $k = 1, 2$.

(II) For $\dim\mathcal{N}(\dot{\mathbf{J}}(s^*)) = \ell \geqslant 2$:

(i) Compute the unit right null vectors $\boldsymbol{\phi}^{(1)}, \ldots, \boldsymbol{\phi}^{(\ell)}$ of $\mathbf{B}(s^*)$ with $\boldsymbol{\phi}^{(k)} = (\bar{\boldsymbol{\phi}}^{(k)^\top}, 0, 0)^\top$, $k = 1, \ldots, \ell$, and solve $\dot{\mathbf{J}}(s^*)\bar{\boldsymbol{\phi}}_0 = -(\mathbf{G}_\beta(s^*)^\top, 0, 0)^\top$ with $\bar{\boldsymbol{\phi}}^{(k)^\top}\bar{\boldsymbol{\phi}}_0 = 0$, $k = 1, \ldots, \ell$, by using sparse SVDPACK [5] (or another suitable package);

(ii) Form $\boldsymbol{\phi}_k = \begin{pmatrix}\bar{\boldsymbol{\phi}}^{(k)}\\ 0\end{pmatrix}$, $k = 1, \ldots, \ell$, and $\boldsymbol{\phi}_{\ell+1} = \begin{pmatrix}\bar{\boldsymbol{\phi}}_0\\ 1\end{pmatrix}$;

(iii) Form trial tangent vectors $\dot{\mathbf{y}}_k(s^*) = \boldsymbol{\phi}_k$, $k = 1, \ldots, \ell$, and $\dot{\mathbf{y}}_{\ell+1}(s^*) = \boldsymbol{\phi}_{\ell+1}$.

References

[1] N. Akhmediev, A. Ankiewicz, Partially coherent solitons on a finite background, Phys. Rev. Lett. 82 (1999) 2661–2664.
[2] E.L. Allgother, K. Gerog, Numerical path following, in: P.G. Ciarlet, J.L. Lions (Eds.), Handb. Numer. Anal., vol. V, Elsevier, 1997.
[3] W.Z. Bao, Ground states and dynamics of multi-component Bose–Einstein condensates, Multiscale Model. Simul. 2 (2) (2004) 210–236.
[4] W.Z. Bao, Q. Du, Computing the ground state solution of Bose–Einstein condensates by a normalized gradient flow, SIAM J. Sci. Comput. 25 (5) (2004) 1674–1697.
[5] M. Berry, Large scale singular value computations, Internat. J. Supercomput. Appl. 6 (1) (1992) 13–49.
[6] T.F. Chan, Deflation techniques and block-elimination algorithm for solving bordered singular systems, SIAM J. Sci. Stat. Comput. 5 (1984) 121–134.
[7] S.L. Chang, C.S. Chien, B.W. Jeng, Liapunov–Schmidt reduction and continuation for nonlinear Schrödinger equations, SIAM J. Sci. Comput. 27 (2007) 729–755.
[8] S.M. Chang, Y.C. Kuo, W.W. Lin, S.F. Shieh, A continuation BSOR–Lanczos–Galerkin method for positive bound states of a multi-component Bose–Einstein condensate, J. Comput. Phys. 210 (2005) 439–458.
[9] S.M. Chang, W.W. Lin, S.F. Shieh, Gauss–Seidel-type methods for energy states of a multi-component Bose–Einstein condensate, J. Comput. Phys. 202 (2005) 367–390.
[10] K.W. Chow, Periodic solutions for a system of four coupled nonlinear Schrödinger equations, Phys. Lett. A 285 (2001) 319–326.
[11] W. Govaerts, Stable solvers and block elimination for bordered systems, SIAM J. Matrix Anal. Appl. 12 (1991) 469–483.
[12] W.J.F. Govaerts, Numerical Methods for Bifurcations of Dynamical Equilibria, SIAM, Philadelphia, 2000.
[13] W. Govaerts, J.D. Pryce, Mixed block elimination for linear systems with wider borders, IMA J. Numer. Anal. 13 (1993) 161–180.
[14] F.T. Hioe, Solitary waves for n coupled nonlinear Schrödinger equations, Phys. Rev. Lett. 82 (1999) 1152–1155.
[15] F.T. Hioe, T.S. Salter, Special set and solutions of coupled nonlinear Schrödinger equations, J. Phys. A: Math. Gen. 35 (2002) 8913–8928.
[16] T. Kanna, M. Lakshmanan, Exact soliton solutions, shape changing collisions, and partially coherent solitons in coupled nonlinear Schrödinger equations, Phys. Rev. Lett. 86 (2001) 5043–5046.
[17] H.B. Keller, Lectures on Numerical Methods in Bifurcation Problems, Springer-Verlag, Berlin, 1987.
[18] Y.C. Kuo, W.W. Lin, S.F. Shieh, Bifurcation analysis of a two-component Bose–Einstein condensate, Physica D 211 (2005) 311–346.

[19] Yueh-Cheng Kuo, Wen-Wei Lin, Shih-Feng Shieh, Weichung Wang, A minimal energy tracking method for non-radially symmetric solutions of coupled nonlinear Schrödinger equations, J. Comput. Phys. 228 (21) (20 November 2009) 7941–7956.
[20] M.K. Kwong, Uniqueness of positive solutions of $\Delta u - u + u^p = 0$ in R^n, Arch. Ration. Mech. Anal. 105 (3) (1989) 243–266.
[21] T.C. Lin, J. Wei, Ground state of n coupled nonlinear Schrödinger equations in $\mathbb{R}^n$, $n \leqslant 3$, Comm. Math. Phys. 255 (2005) 629–653.
[22] M. Mitchell, Z. Chen, M. Shih, M. Segev, Self-trapping of partially spatially incoherent light, Phys. Rev. Lett. 77 (1996) 490–493.